Composites Part C: Open Access 15 (2024) 100527

Contents lists available at ScienceDirect

Composites Part C: Open Access

journal homepage: www.sciencedirect.com/journal/composites-part-c-open-access

Lightweight 3D-printed heaters: design and applicative versatility

Francesca Aliberti [a,*], Andrea Sorrentino [b], Barbara Palmieri [c], Luigi Vertuccio [d], Giuseppe De Tommaso [e], Roberto Pantani [a], Liberata Guadagno [a], Alfonso Martone [c,*]

[a] *Department of Industrial Engineering, University of Salerno, Via Giovanni Paolo II, Fisciano, SA 84084, Italy*
[b] *Institute for Polymers, Composites, and Biomaterials (IPCB-CNR), Via Previati n. 1/E, Lecco 23900, Italy*
[c] *CNR-IPCB Institute for Polymers Composites and Biomaterials, Consiglio Nazionale delle Ricerche, P.le E Fermi 1, Portici 80055, Italy*
[d] *Department of Engineering, University of Campania "Luigi Vanvitelli", Via Roma 29, Aversa 81031, Italy*
[e] *A.T. M. - Advanced Tools and Moulds srl, Zona Industriale EX-INDESIT stab. 15 Gricignano di Aversa (CE), Italy*

ARTICLE INFO

Keywords:
Versatile 3D-printed heater
Design optimization
Joule heating performance
FEM analysis

ABSTRACT

This paper proposes a new strategy for designing a 3D-printed heater that can overcome some criticalities of current commercial heater devices for application in the transport and energy sectors. A semiconductive nanocomposite material, acrylonitrile-butadiene-styrene filled with carbon nanotubes (ABS-CNT), was processed via Fused Filaments Fabrication (FFF). The printing was set to favor the current flow along the printing direction, consequently increasing the material's electrical conductivity. 3D-printed heater geometry, equivalent to several electrical resistances (resistive branches) connected in parallel, was optimized by varying the width, thickness, lengths, and number of branches. The adopted approach resulted in a flexible and scalable low-equivalent resistance value heater. Moreover, the optimized heater's flexibility allows it to be integrated into a curved fiberglass composite. Joule heating tests were experimentally performed and theoretically simulated by a multi-physics model. The numerical prediction resulted in good agreement with the experimental data. The results encourage the application of 3D-printed heaters as functional patches for the thermal management of different devices/components, including complex-shape composite structures.

1. Introduction

In the electrification era, electrothermal heating, based on the Joule effect, has gained a lot of interest in the industrial field. De-icing in the automotive, aeronautical, building, and renewable energy sectors [1–3] is one of the main applications. Ice accumulation on wigs airplanes, on the car windshield or bumper, on wind turbine blades, or the roof of houses increases the structure's weight [4]. Moreover, in the case of transportation means and wind turbines, the presence of ice causes a considerable change in the shape and roughness of the surface with negative effects on their stability, safeness, aerodynamics, and energy performance [3,5–7]. The possibility of having a heater on board directly integrated into the structure represents a huge advantage since the de-icing process could be as simple as pushing a button to remove the ice. In addition, the heating system could be wirelessly controlled for large outdoor installations, such as wind turbine blades. However, electrothermal heaters are not limited to de-icing applications; they could be used in the out-of-autoclave processes for the thermal curing of thermoset resin [8–11] or for resistance welding and induction welding of thermoplastic/thermosetting composites [12–16]. In the first case, the traditional curing cycle in the autoclave is a long, time-consuming process characterized by a great loss of energy in the convective heating [17,18]. Electrothermal heaters can be directly embedded into the molds as an effective heating system for managing thermal gradients that can affect the quality of the final product [19]. Electrothermal active materials are also suitable for promoting adhesion in resistance welding applications. Heat is generated by the Joule effect when an electrically conductive heating element (often a nanocomposite thermoplastic film) located at the weld interface between two composite adherents is connected to a power source, while pressure is applied to the welding stack to promote the intimate auto-adhesion during the melting and consolidation phases [13]. In addition, the chance to control the shape and electrical conductivity of nanocomposite webs and grids could enable using this material as a susceptor in induction welded joints. In the latter case, the heater is activated by eddy currents caused by an alternating magnetic field [20,21]. Therefore, the capability to

---

* Corresponding authors.
E-mail addresses: faliberti@unisa.it (F. Aliberti), alfonso.martone@cnr.it (A. Martone).

https://doi.org/10.1016/j.jcomc.2024.100527

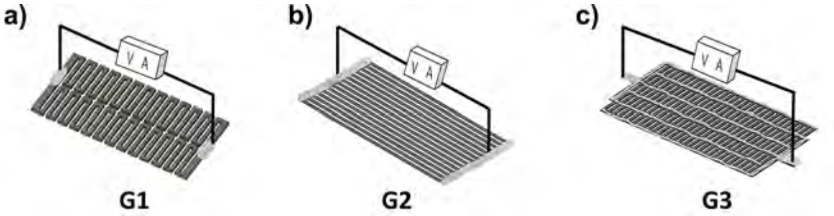

Fig. 1. 3D printed resistors: (a) geometry 1 (G1), (b) geometry 2 (G2), (c) geometry 3 (G3).

tune the electrical conductivity of the nanocomposite and the final shape is pivotal for enabling many applications. An in-depth analysis of the joule heating effect is mandatory to design and manufacture efficient electrothermal heaters. The main phenomenology related to the Joule effect is the conversion of electrical energy into thermal energy inside the material, which is related to electron inelastic collisions with phonons, impurities, or defects; the higher the collisions, the higher the energy dissipated (as heat). To the best of the authors' knowledge, most of the electrothermal heaters available on the market or used in the industrial fields are metallic. The electrothermal conversion efficiency is very low when the heater is made of a metallic material [22]. The related corrosion problems cause a loss of mechanical properties and high maintenance costs. Furthermore, metals lead to heavy heaters with high integration costs, making their use disadvantageous [23]. High-conductive metals have been recently replaced with resistance heating elements [24] made of conductive composite materials [25–33] to overcome the limitations mentioned above. Among the different processes already used for producing thermoplastic nanocomposite heaters (such as compression molding, injection molding, and solvent casting), Fused Filament Fabrication (FFF) emerges for several advantages. It is a 3D-printing technology in which a thermoplastic material in a spooled filament is fed into the printing head, extruded, and deposited layer by layer according to the designed geometry [34]. Firstly, the final object's shape must be modeled using CAD (Computer Aided Design) software. Then, the printing parameters are set in the CAM (Computer Aided Manufacturing) phase, allowing us to see how the object will be printed in advance. The FFF process offers the possibility to directly depose the nanocomposite material in the interested area according to the designed conductive path, reducing the scalability issues in the industrial field [35,36] and contributing to the manufacturing of components with on-demand properties [37]. Other additional advantages are: (i) the absence of molds for complex geometry and thus reduced tooling costs, (ii) the possibility of using simultaneously two different kinds of thermoplastic materials for hybrid structures, and (iii) no materials waste. The FFF process could solve overproduction, reworking, waiting and delays, and overprocessing, typical production line issues related to producing prototypes at an industrial scale when a new product is experimented [38].

Several 3D-printed heaters have been produced via the FFF process in the literature using carbon-based filler in thermoplastic polymers [39–42]. The addition of high-conductive carbon-based nanofiller, such as carbon nanotubes (CNT) [43], graphene nanoplates (GnP) [44], and carbon black [45], into the insulator polymeric matrix, allows for an increase in the electrical conductivity of the final nanocomposites, a key aspect to guarantee the Joule heating effect when an electrical stimulus (e.g. power or voltage) is applied [46,47]. Moreover, when nanocomposite materials are applied in the FFF process, anisotropic effects on mechanical and electrical properties are obtained [48,49]. However, electrical anisotropy is effectively reached when properly selecting the printing path. More in detail, starting from a semiconductive thermoplastic nanocomposite, developing a low-resistance heater to heat up at low voltage values is a challenging goal.

Table 1
Printing parameters.

Printing parameter	Value
Extrusion temperature	250 °C
Bed temperature	80 °C
Height of the first layer	0.3 mm
Layer thickness	0.2 mm
Infill density	100 %
Printing speed	80 mm/s
Nozzle diameter	0.4 mm

In most cases, the strategy consists of increasing the conductive filler content beyond the electrical percolation threshold to ensure efficient Joule heating at low voltages [50]. However, if the filler content must be kept constant to meet other requirements (such as thermal conductivity and structural and mechanical properties), it is necessary to guarantee self-heating functionality without changing the composition of the material. In this context, the anisotropic effect of the FFF process on the electrical properties can be exploited to guarantee a high electrical conductivity along the printing direction [51].

Among the wide range of thermoplastic nanocomposites applied in the FFF process, ABS filled with CNT is one of the most used because its high glass transition temperature allows for higher temperatures [52], especially in the electrothermal applications mentioned before. In addition to this advantage, superior chemical properties, excellent toughness, and good dimensional stability [53] make nanocomposite ABS particularly suitable for integration into high-performance composites.

In the present study, all these aspects have been investigated. ABS filled with CNT has been used to design a flexible and scalable 3D-printed electrothermal heater. First of all, the effect of the printing direction on the anisotropic electrical properties of ABS-CNT material has been demonstrated to be crucial to increasing the electrical conductivity of the printed heater. Not only process parameters but also the geometry of the heater has been optimized to meet the application requirements in terms of power/voltage limit, flexibility, and scalability on large-area elements. Evidence of the actual applicability of the produced 3D printed heater has been given by its successful integration into composite structures made of fiberglass (GFRP) layers without compromising the Joule heating performance. Moreover, Finite Element Method (FEM) has been used to simulate the experimental data of Joule heating tests. The obtained results suggest that the proposed design strategy is useful for predicting both the electrical resistance value (by electrical model) and Joule heating performance (by FEM analysis) of the electrothermal printed heater.

In this way, the current paper represents a step forward in the design strategy of electrothermal heaters produced via the FFF process. Concerning the current literature [11,54,55], FFF potentialities have been exploited to obtain both better electrical properties without changing the material composition and the scalable geometry of the heater. In addition, from the industrial point of view, this geometry can be easily integrated into flat or curved composited structures by exploiting its mechanical flexibility or directly depositing the material from the printing head on the glass fiber-reinforced polymer (GFRP) substrate.

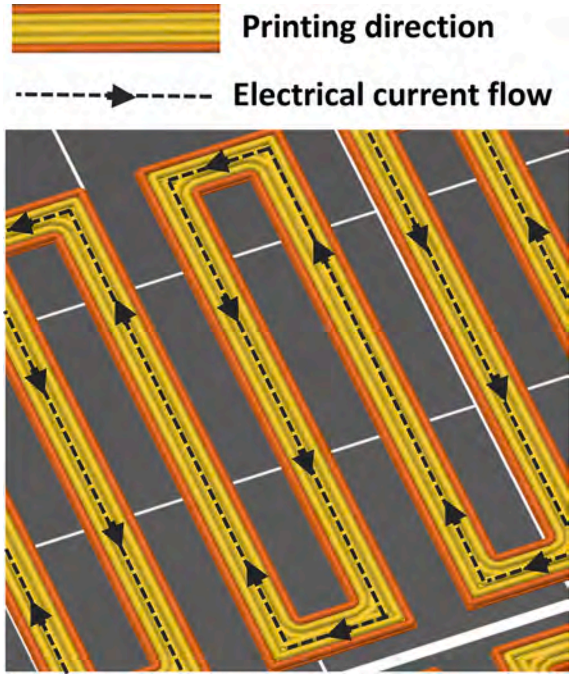

Fig. 2. Visualization of the perimeter infill pattern and current flow direction.

2. Materials and methods

2.1. Printing process

ABS filled with carbon nanotubes (ABS-CNT) was supplied by 3DXTECH Additive Manufacturing. The diameter of the pre-printing filament is 1.75 mm. Nanofiller content indicated in the technical datasheet is less than 10 % by weight. This information was verified via thermogravimetric analysis reported in Fig. S1 of the Supplementary Material (S.M.). The original Prusa i3 MK2 3D printer (Prusa Research) was used to produce three different geometries of resistors (Fig. 1).

CAD files were prepared in Fusion 360 and exported as .stl files. Printing parameters, summarized in Table 1, were set on the Slic3r Prusa Edition (Prusa Research) software and kept equal for all the experimented samples. All printed parameters were optimized during preliminary printing tests to guarantee good final quality of the heater. As suggested by some papers in the literature [56–59], layer height and extrusion temperature are crucial to obtain a low surface roughness together with printing pattern and infill rate. Limiting FFF defects (e.g. porosity [60]) related to the appropriate choice of the parameters is the first step to ensure uniform temperature distribution during the Joule heating test. In the specific case of the present study, the bed and extrusion temperature were set based on material thermal properties reported in the S.M. Since ABS-CNTs is an amorphous thermoplastic polymer having a glass transition temperature at 110 °C (see Fig. S1b), it is completely softened at about 100 °C beyond T_g. ABS-CNT shows a suitable FFF processability in terms of viscosity at the outlet of the nozzle at a temperature of 250 °C [61] set as extrusion temperature. Moreover, the bed temperature, fixed at 80 °C, allows thin and large objects to be printed without having detachment from the printing bed and deformations (e.g., warpage or shrinkage). A heated bed improves material adhesion and lowers the cooling rate, allowing the material to relax internal stresses [62]. The layer height of 0.2 mm is commonly set when a nozzle diameter of 0.4 mm is used [52]. However, the first layer height has been increased to 0.0 3mm to easily remove thin samples from the printing bed at the end of the process without compromising the quality of the surface attached to the bed. Finally, a printing speed of 80 mm/s has guaranteed good printing quality without prolonging the process time.

Geometry 1 (G1), schematized in Fig. 1a, is inspired by commercial heater foil usually made of thin metallic wire. According to the position of electrical contacts, it can be schematized as two resistances in parallel from an electrical point of view. Geometry 2 (G2) has been obtained from G1 by increasing the number of resistances in parallel from 2 to 15 and reducing their length from 73.6 cm to 10 cm. G2 configuration is composed of straight branches to cover the same heating area (30 cm^2) that has been kept constant. Similarly, Geometry 3 (G3) was designed by continuously increasing the number of branches from 15 to 150 and reducing their length from 10 to 1 cm resulting in a comb configuration of electrical contacts. Engineering drawings (top and front view) of 3D printed resistors are provided in Fig. S2 of the S.M.

The samples' infill was obtained by increasing the number of perimeters so that each layer was completed by concentrically repeating the perimeter, as schematized in Fig. 2, without using Prusa Slic3r's proposed infill patterns. This choice favored the flow of electrical current in the same direction as the printed filaments.

2.2. Integration of 3D printed heater in the fiberglass composite

The G3 printed heater was integrated into a fiberglass composite to prove its applicability as a heating element for de-icing applications. Two different molds were used to obtain a flat and curved sample. The assembling procedure for fiberglass composites containing G3 is schematized in Fig. 3.

A 3D-printed heater having long electrical contacts was introduced in the middle plane of a symmetric system consisting of two sandwich structures placed on the top and the bottom of the heater (Fig. 3a). More in detail, each sandwich structure was composed of four fiberglass prepreg plies (Krempel BD 2808, twill 2,2) [63] arranged in a stacking sequence of (0°/90/0°/90°) as schematized in Fig. 3a. To apply electrical voltage to the 3D-printed heater, longer electrical contacts were preliminary designed in the CAD phase in such a way as to prolong them out of the fiberglass composite. A vacuum bag system was used to compact the composite structure and reduce the voids in the final sample during the curing process performed in an oven at 80 °C for 3h.

The process parameters were set up in such a way as to preserve the integrity of the ABS-CNT heater; the GFRP prepreg was selected since it can be consolidated well below the softening temperature range of the heater, ABS-CNT has its glass transition at around 110 °C and remarkably soften around 250 °C. Differential Scanning Calorimetry, DSC, thermograms are shown in Fig. S1b.

The complete procedure is summarized in Fig. 3b. Detailed images of the 3D-printed heater integrated into the fiberglass structure are provided in Fig. S3.

2.3. Morphological analysis

Morphological investigation was performed on ABS-CNT printed samples after etching treatment described as follows. To better investigate the distribution of CNT, part of the polymeric matrix was removed using an oxidizing solution (etching solution) consisting of 1.0 g potassium permanganate added to 95 ml sulfuric acid (95–97 %), and 48 ml orthophosphoric acid (85 %). Printed samples were left in the etching solution for 24 h under stirring at room temperature. Subsequently, the samples were washed in a cold mixture of two parts volume of concentrated sulfuric acid and seven parts water and then in a 30 % aqueous hydrogen peroxide solution. Finally, once they were washed with distilled water, the samples were dried under vacuum for 2 days.

SEM micrographs were obtained using the SEM LEO 1525 (Carl Zeiss SMT AG, Oberkochen, Germany) microscopy. The printed samples were firstly fractured in liquid nitrogen to ensure no distortion during the rupture and then covered with a 250-Å thick gold film by using a sputter coater (Agar mod. 108 A).

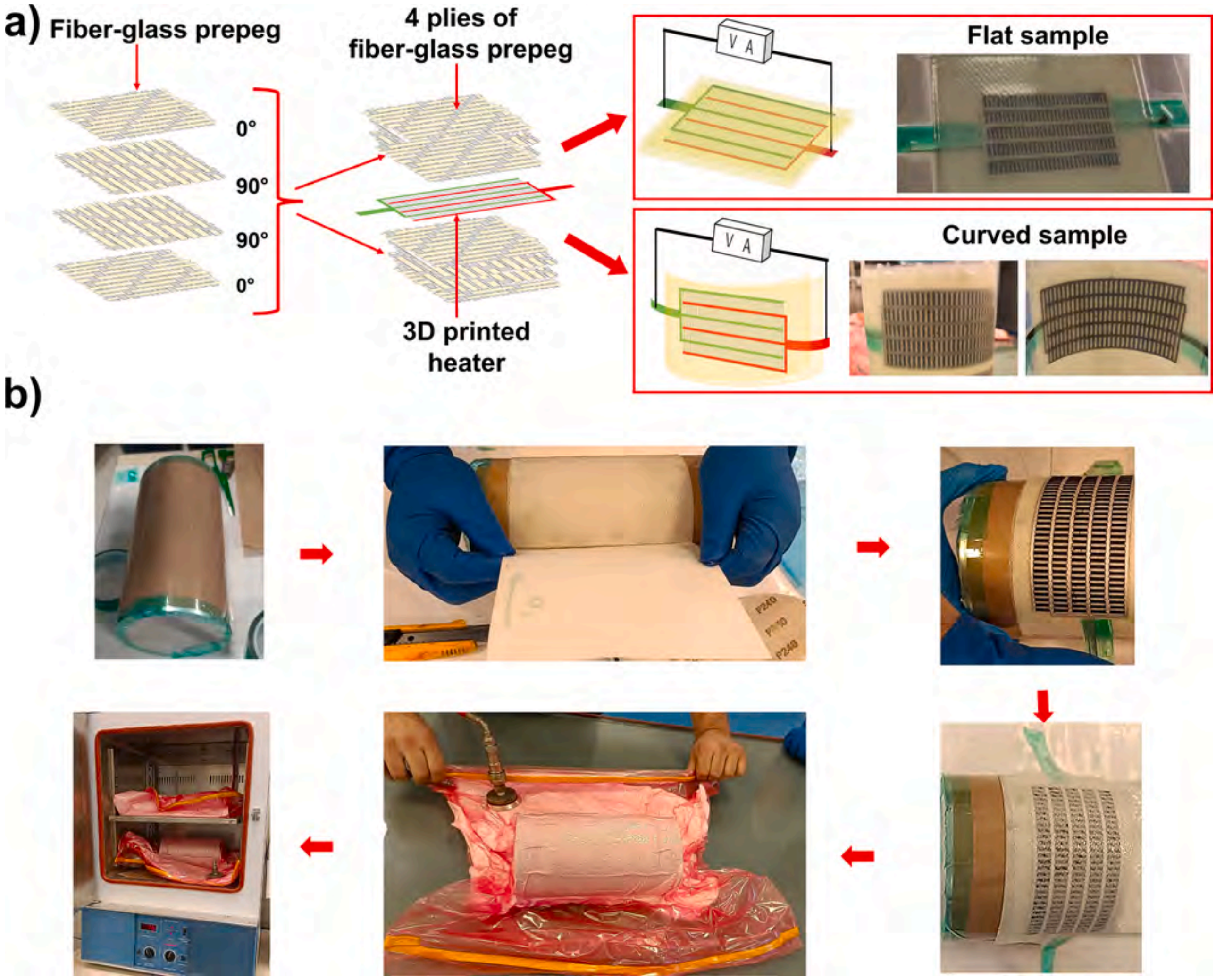

Fig. 3. (a) Scheme of integrated 3D printed heater in the fiberglass layered structure, (b) integration and manufacturing procedure of the composite structure.

2.4. *Electrical characterization and Joule heating tests*

The electrical resistance of the 3D printed geometries was obtained as the slope of the current-voltage (I–V) characteristics. On each sample, the electrical contacts were realized with silver paint (RS 196–3600, RS PRO, Corby, UK) whose electrical conductivity of 10^5 S/m is largely higher than that of nanocomposite material. An electrometer, Keithley 6517A (Keithley Instruments, Cleveland, OH, USA), was used as a power supply from 0 to 25 V in 10 steps. At each voltage value, the electrical current was measured five times with a Multimeter 3458A (Agilent, Santa Clara, CA, USA), and the resulting mean value was reported in the I-V graph at the corresponding set voltage value. This procedure was repeated also from 25 to 0 V to exclude the hysteresis phenomenon. Joule heating tests were carried out by applying a determined voltage value and measuring the increase in the temperature over time for 1200 s. Meanwhile, the electrical resistance variation was recorded to investigate its stability during the heating of the material. The utilized equipment for the Joule heating test is schematized in Fig. 4e described in detail in Ref. [64]. Joule heating tests were performed on the 3D-printed heater and the fiberglass composite in the air at room temperature.

2.5. *Coupled electro-thermal analysis for the heater*

In this paper, a three-dimensional numerical model of a 3D-printed heater has been developed. The model, realized by COMSOL Multiphysics software, consists of the Heat Transfer in the Solids interface coupled with the Electric Currents interface from the AC/DC Module. The analysis was carried out by defining as input the voltage onto the 3D-printed heater, the temperature field was computed as the effect of resistive heating of the element and as a result of heat exchange with the ambient.

3. Results and discussion

3.1. *Morphological results*

Morphological investigation is useful for understanding the electrical properties of the printed samples at the microscopic scale. SEM micrographs (Fig. 5a, b) reveal the presence of carbon nanotubes inside the nanocomposite ABS-CNT and the effect of printing parameters on the material's morphology.

In Fig. 5a, the printing direction is well evidenced by the interfacing zones between adjacent filaments. These interfacing zones are responsible for the anisotropic properties of the 3D-printed artifacts. It is easy to imagine that the number of electrical contacts between the bundles of carbon nanotubes (shown in Fig. 5b) along a single printed filament is higher than the electrical contact between one printed filament and the adjacent one. This consideration aligns with the current literature. Dul et al. [65] investigated the difference between the resistivity values in the XY direction and the Z direction for 3D-printed ABS/CNT samples at different filler concentrations. The authors found that the electrical

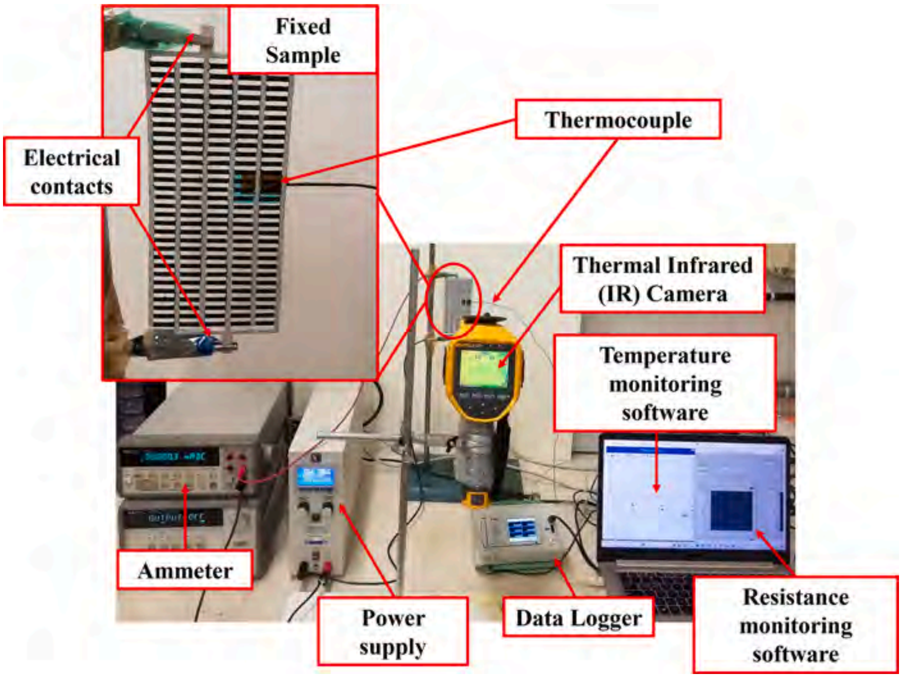

Fig. 4. Picture of instrumentation used for Joule heating test.

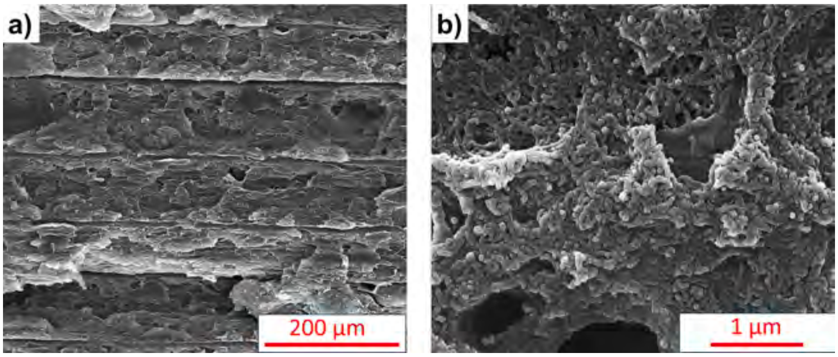

Fig. 5. SEM micrographs on 3D-printed samples: (a) adjacent filaments along printing direction, (b) carbon nanotubes along a single printed filament.

conductivity of the through-layer was of about 2–3 orders of magnitude higher than the cross-layer value. Similarly, in previous work [51], the authors of the present paper demonstrated that the electrical conductivity when the current flows in the direction perpendicular to the printed filaments is about two orders of magnitude lower than the electrical conductivity of a sample where the current follows the printing direction. More in detail, the electrical conductivity increases from 7.34×10^{-2} when the electrical current flows perpendicular to the printed filaments to 1.22 S/m when the current is parallel to the printed filaments. Based on this previous finding, considering the position of electrical contacts (see Fig. 1) and the infill pattern (see Fig. 2), the electrical current flows in the same direction as the printed filaments. This approach allows to reach higher power with lower voltage values.

3.2. *Electrical results and Joule heating tests on the heaters*

In the present work, the composition of the material has been kept unchanged while the reduction of electrical resistance of the printed samples has been obtained firstly by properly choosing the process parameters and then by optimizing the geometric parameters. A specific print strategy was followed during the sample fabrication: (i) the filament deployment paths were defined according to the current direction, and (ii) the infill was set linearly along the perimeter with 100 % density. The rationale for the strategy was to promote the electrical current flux without hindrance and take advantage of CNT orientation during the extrusion stage. The printing instructions (gcode/CAM) were carefully generated for all the geometries, accounting for the current flow direction (Fig. 2). Starting from a commercial model, the geometries of the three 3D-printed resistors were obtained as a result of a geometric optimization process described hereafter. To compare them in terms of electrical resistance, the printing area occupied by the samples has been kept constant and equal to the value of 30 cm^2. The equivalent resistance value (R_{eq}) of the three considered geometries (G1, G2, and G3) is described by the following equation:

$$\frac{1}{R_{eq}} = \sum_{i=1}^{n} \frac{1}{R_i} \tag{1}$$

where $R_i$is the electrical resistance value of each branch composing the whole resistance and n is the number of resistive branches in parallel. When the branches in parallel have the same resistance value (R), the Eq. (1) can be re-written as follows:

$$R_{eq} = \frac{R}{n} \tag{2}$$

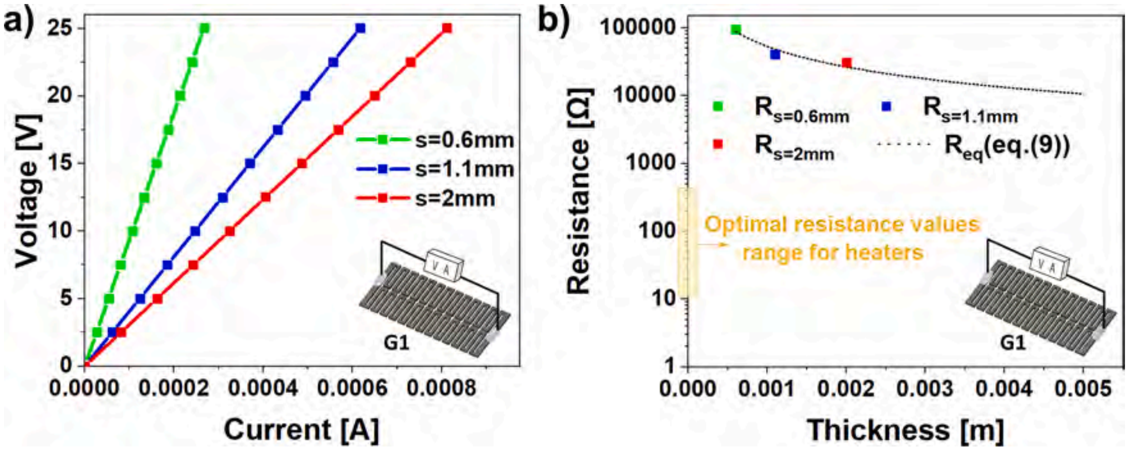

Fig. 6. (a) IV characteristics of the three samples of G1 having different thicknesses, (b) Resistance trend with the thickness of the sample G1 and comparison with G2 and G3 resistance values.

According to the second Ohm's law:

$$R = \rho \ * \frac{L}{W * s} \tag{3}$$

where ρ is the electrical resistivity of the material, *L* is the length, *W* the width and *s* the thickness of the sample. By combining the Eq. (2) with Eq. (3), it is possible to obtain a simple and effective equation to apply in case of equal resistances in parallel:

$$R_{eq} = \frac{1}{n} * \rho \ * \frac{L}{W * s} \tag{4}$$

Since the material composition remains unchanged, the electrical resistivity is the same for all three configurations. It is necessary to specify that the material's electrical resistivity in the form of spooled filament is different from its value after the passage through the printing nozzle. The phenomenon of carbon filler, especially carbon nanotube, alignment in the printing direction at the nozzle outlet has already been studied in the literature [66–69]. In a previous paper [51], the authors found out that the electrical conductivity of a single printed filament (1.19×10^1 S/m) is about three orders of magnitude higher than the electrical conductivity of the spooled filament before the printing process (6.88×10^{-2} S/m). Moreover, morphological results shown in paragraph 3.1 suggest that the printing direction could affect the electrical properties of the materials although its composition remains the same since preferential paths are created inside the printed sample. This evidence implies that the term ρ in Eq. (4) must be referred to the electrical resistivity of the material after the printing process. When the electrical current flows in the same direction as the printed filament the resistivity of the ABS-CNT is about 0.8 Ω*m [51]. This value was obtained by performing a current/ voltage (IV) characterization on printed specimens with an aligned infill pattern on each layer and positioning the electrical contacts so that the current flow was parallel to the printed filaments. Since all tested samples were printed in such a way that the electrical current was parallel to the printing direction, this value of resistivity was used to verify the validity of the model described by Eq. (4). Three samples having G1 configuration with different values of thickness were printed. IV characteristics of these samples are reported in Fig. 6a.

Fig. 6a shows that 3D-printed resistors with G1 configuration behave like ohmic resistances. This result allows the application of Eq. (3) for the studied systems. According to the position of electrical contacts, as shown in Fig. 1a, G1 can be schematized as two resistances in parallel. As expected by Eq. (4), based on the concept of electrical resistance in parallel also for 3D printed resistors, by increasing the thickness of the samples, the electrical resistance tends to decrease. Further proof of the validity of Eq. (4) for 3D printed heater, comes from the graph reported in Fig. 6b. The points indicate the resistance values of the three samples (with G1 shape and having different thicknesses) obtained as the slope of the IV curves of Fig. 6a, while the black curve is the model of Eq. (4), obtained by using the geometric parameters L, W, s (Table 2) of the samples, the electrical resistivity of the material when the current flows along the printing direction (0.8 Ω*m) and considering two resistance in parallel ($n = 2$). Since the experimental data are fitted by the electrical model of Eq. (4), 3D-printed resistors can be described as ohmic resistance in parallel. Another suggestion can be deduced from the black curve in the Fig. 6b. Although the increase of the thickness implies a decrease in the equivalent resistance value, it would not be sufficient to reach the suitable interval of resistance values for heaters to be activated by the power suppliers commonly available in the different application fields. For instance, if the heater has to be applied as a de-icing system of the modern aircraft, the power supplier available on board can dispense 28V and 110V [70], while if this system is thought to be inserted as heating elements in the civil building for the de-icing of the roofs in cold regions, the electrical source could be the domestic electric grid that is 230V in Europe and 120V in the United States [71]. Also, the electric voltage available on board for automotive applications is 12 or 48V [72]. In the case of high resistance value, a technological limit is born. On the other hand, at low resistance values (e.g. metallic resistors) the conversion efficiency from electrical to thermal energy is attenuated [8]. Based on validated Eq. (4), a geometric optimization of 3D printed heaters has been carried out to adapt their electrical resistance value to the technological limits previously described exploiting the advantage of free-form producing of 3D printing. In fact, once the geometry has been designed, the FEM analysis can be performed on the same CAD model to verify if the electrical source available in the application field is

Table 2
Comparison of heating performances of the three experimented 3D-printed heaters.

	G1	G2	G3
R_{eq} [Ω]	30,834	823	30
P [W]	4	12	11
ΔV [V]	350	100	18
T_{ss} [°C]	45	100	76
n	2	15	150
L [cm]	73.6	10	1.25
s [mm]	2	2	0.5
W [mm]	2	2	2

*R_{eq} is the total equivalent electrical resistance of the investigated geometries, P is the electrical power, ΔV is the applied electrical voltage, T_{ss} is the steady-state temperature, n is the number of resistive branches in parallel, L is the length of each branch, s is the thickness and W the width of each branch.

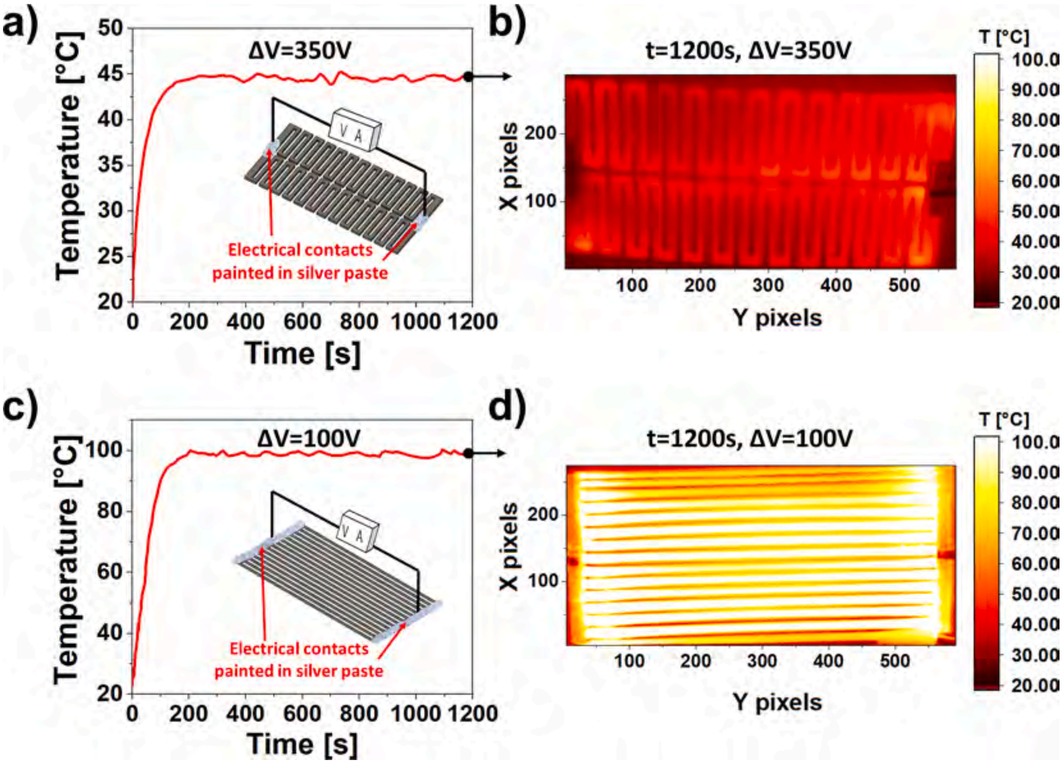

Fig. 7. (a) Scheme of geometry 1 (G1); (b) temperature profile during Joule heating test at 350V and temperature distribution at 1200s of G1 configuration; (c) scheme of geometry 2 (G2); (b) temperature profile during Joule heating test at 100V and temperature distribution at 1200s of G2 configuration.

sufficient to reach a determined temperature. The G1 sample (see Fig. 7a) shows an electrical resistance value of 30,834 Ω. As expected, to activate a heater with a high resistance value, a high voltage value must be applied to obtain an appreciable increase in the temperature. Joule heating tests on this sample (Fig. 7b) revealed a steady state temperature of 45 °C is reached by applying 350V, a voltage value out of the application mentioned above ranges. In any case, the thermal map in Fig. 7 shows a homogeneous distribution of temperature on the G1 sample surface.

To reduce the resistance value of the 3D printed heater, the optimization of geometric parameters was carried out on the base of Eq. (4) by keeping constant the printed area. More in detail, the G2 configuration as described in the paragraph 2.1 was obtained by increasing the number of branches in parallel and decreasing their length, while the thickness value was the same for both G1 and G2 (s = 2mm). This modification of the heater geometry has led to a decrease in the resistance value of two orders of magnitude. G2 heater shows a resistance value of 823 Ω that falls in the desired range of values for the resistors (see Fig. 6b). In fact, by applying a DC voltage of 100V a steady state temperature of 100 °C was reached as shown in Fig. 7c. Even in this case, a uniform temperature distribution was obtained (see Fig. 7d). Higher voltages would lead to higher temperatures not compatible with the thermal stability (glass transition temperature about 110 °C) of the ABS polymer (S.M. reports thermal properties of selected materials). The topological modification of the element allowed to achieve a higher efficiency in converting power in heat increasing the equilibrium temperature about 2 times and requiring a power supply of only 100 V. Even if the G2 configuration has improved heating performance with respect to the previous configuration (G1), another aspect to take into account for further integration in subsystems (i.e. curved shape parts) is flexibility. Fig. 9a, b compares the flexibility of G1 and G2 samples.

G2 configuration turns out too stiff to be integrated even in parts with little curvatures. According to the literature [73,74], a thicker heater would show better heating performance than a thin one considering the same filler content. However, to get flexibility, it is necessary to reduce the thickness of the sample from 2 mm to 0.5 mm. To compensate for the rise of electrical resistance on the base of the Eq. (4), the number of branches was increased from 15 to 150 while their length was reduced to 1 cm. The shape of the heater appears as a series of small resistive branches connected in parallel. This new geometrical

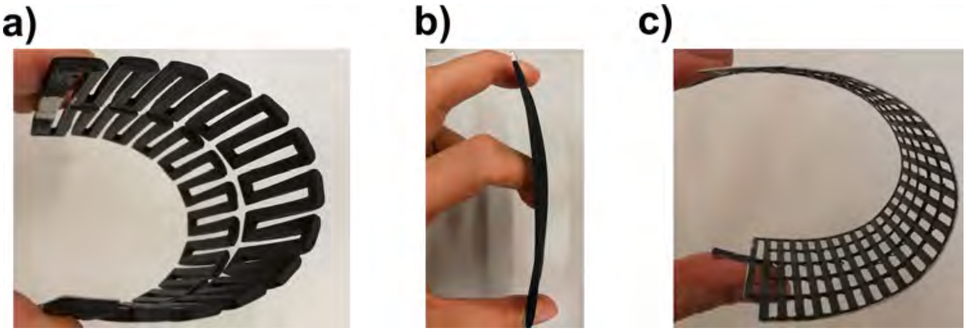

Fig. 8. Images of the printed heaters show their flexibility: (a) G1, (b) G2, (c) G3.

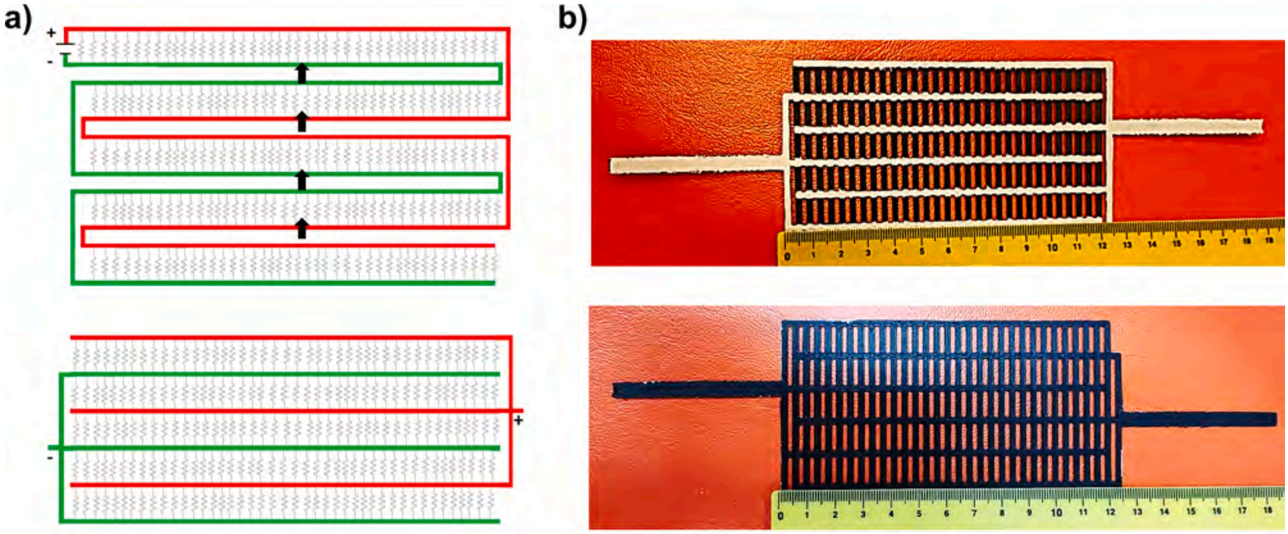

Fig. 9. 3D printed heater with G3 configuration: (a) scheme of comb structure; (b) images of both sides of the G3 sample.

configuration (G3) requires a different electrical connection to supply the current to all the elements. By folding the long series of small resistive strips in parallel and overlapping the equipotential surfaces of the electrical contacts, a comb structure was obtained as schematized in Fig. 9a.

The green and red colors in Fig. 9a evidence the two electrode paths necessary to bring the same potential difference to every branch composing the heater G3. In the real sample (Fig. 9b), the electrodes were obtained by distributing a thin layer of silver paste on the same sample regions evidenced in the scheme of Fig. 9a. Since the thickness of the 3D-printed heater with a flexible G3 shape is very low, the silver paint used to create the equipotential surfaces for electrical contacts (red and green lines in Fig. 9a) was deposited only on one side of the sample (see Fig. 9b). Thanks to the last geometrical optimization, the electrical resistance achieved by the G3 was lowered to the outstanding value of 30 Ω allowing it to reach an equilibrium temperature of 76 °C with a DC voltage of only 18V (see Fig. 10). In such a way, not only the Joule heating performance of G3 was enhanced with respect to that of the G2 sample but also exceptional flexibility (Fig. 8c) was obtained. Joule heating performance (applied voltage ΔV and power P, steady-state

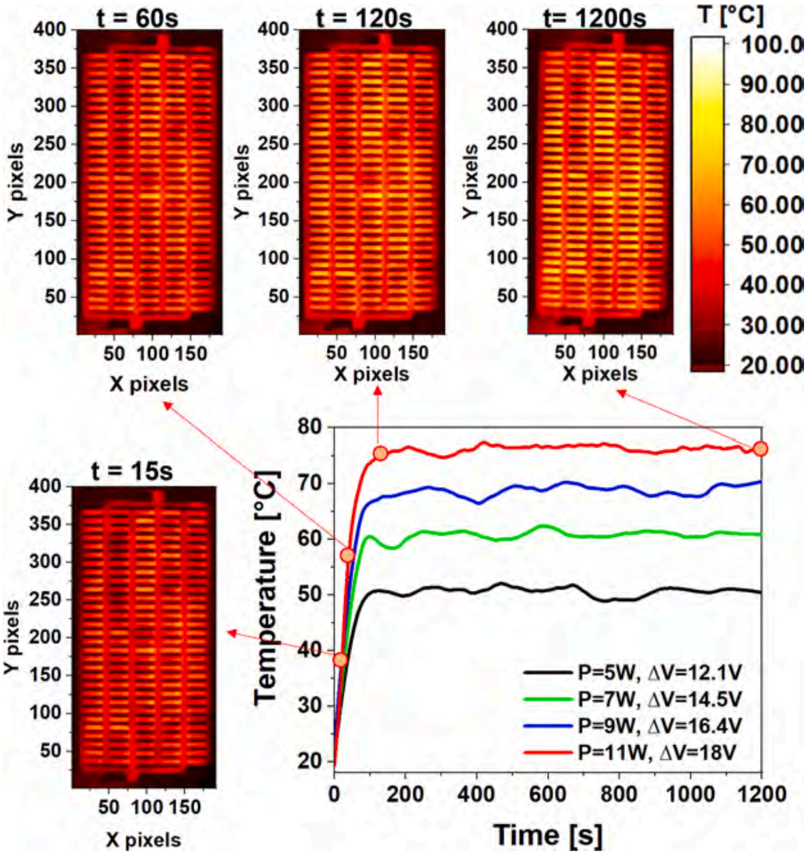

Fig. 10. Joule heating performance of 3D printed heater with G3 and low resistance value.

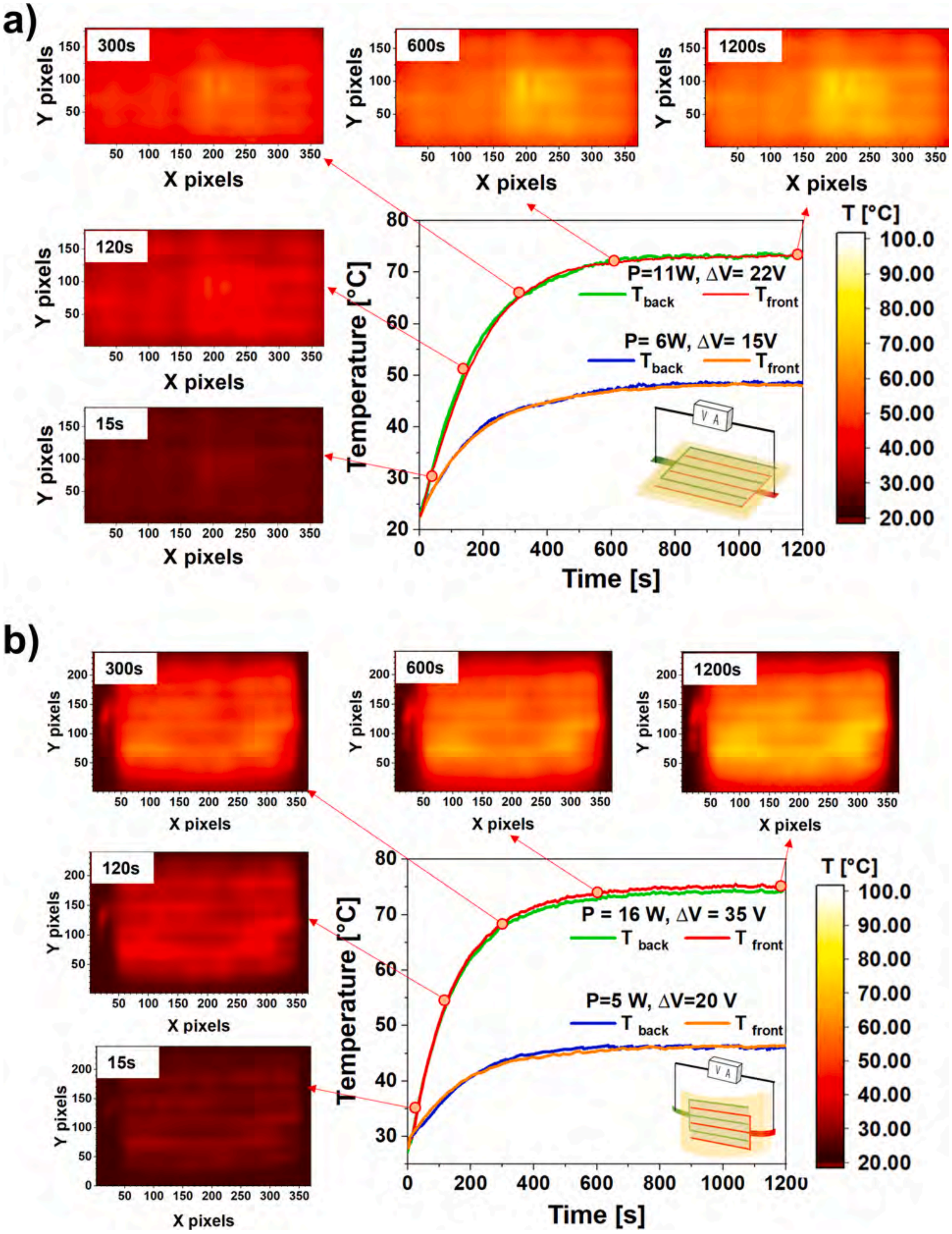

Fig. 11. Joule heating performance of flat (a) and curved (b) samples of GFRP/G3.

temperature T_{ss}) and geometrical parameters of the three considered heaters (W, L, s, n) are summarized in Table 2.

In the light of better heating performance of the G3 configuration, a more detailed investigation is shown in Fig. 10.

Fig. 10 shows the results of Joule heating tests performed on the sample with G3 configuration in terms of temperature profile and surface temperature mapping. By increasing the voltage applied, the power, and thus the heat generated inside the sample, increases obtained higher temperatures. Similarly, the heating rate evaluated in the first temperature interval of 20 °C for all the curves of Fig. 10 passes from 30 °C/min

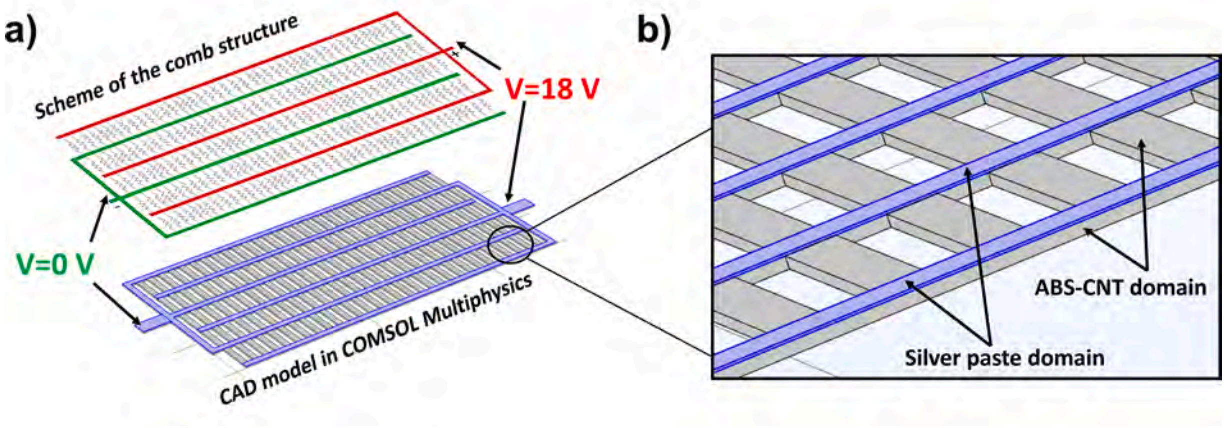

Fig. 12. (a) Scheme of electrical contacts path on CAD model in COMSOL Multiphysics, (b) ABS-CNT and silver paste domains.

to 114 °C/min by increasing the voltage from 12.1V to 18.2V, respectively. The heating performance of the G3 configuration is comparable and even better than other examples of 3D-printed heaters found in the literature [11,75,76] thanks to the optimization of the geometry that allows for reducing the electrical resistance. Moreover, thermal maps, reported only for the higher applied voltage, reveal a homogeneous temperature distribution on the sample surface during the whole duration of the heating test. This result is not obvious if the complexity of the geometry is considered. Kin et al. [77] tried to uniformly heat a 3D-printed honeycomb structure. However, heat generation was concentrated near the electrodes where higher temperatures were reached. By increasing the voltage applied, melting occurred at the point where the power supply was connected. This example highlights two important challenges overcome in the present study: on the one hand, the proper design of the electrodes according to the geometry of the sample, and on the other hand, the reduction of the 3D printing defects. Regarding the first aspect, in the present study, electrodes (made of silver paint) have been designed in such a way as to bring the same electrical potential at the extremes of each branch. However, this is not sufficient because if a defect (air voids, filaments discontinuity, etc.) occurs in a branch during the printing process, during the Joule heating test, that branch will show a lower temperature due to the increase in the local resistance caused by the defect which obstacles the current flow. Finally, the good homogeneity in the temperature distribution testifies to the good printing quality of the heaters.

3.3. Joule heating tests on the G3 heater integrated into fiberglass composite

The topological optimization carried out in this work paves the way for the development of scalable heating elements on a large scale. G3 configuration is an example of a flexible and scalable low-resistance heater. More in detail, if the heating area becomes bigger, the comb structure can be repeated following the schematization of Fig. 10a. In this way, the number of branches would be increased, thus their length will increase to maintain the equivalent resistance value constant (according to equation (9)). Another interesting feature of the G3 sample is its flexibility which is appreciable in Fig. 9c. This aspect allows it to be applied on curved structures, such as the leading edge of airplanes for de-icing applications, otherwise, the comb geometry could be directly printed on the structure to be heated whatever is its geometry thanks to the additive manufacturing advantages. The optimized G3 heater was integrated into a fiberglass (GFRP) structure obtaining a self-heating composite (GFRP/G3) for potential structural applications. A curved mold was used to exploit the flexibility of the G3 configuration and mimic the shape of the leading edge. Joule heating performances of flat and curved GFRP/G3 systems are reported in Fig. 11.

A thermocouple on each surface of the fiberglass composite was placed to record the temperature profiles on both sides of the flat and curved samples to verify the presence of possible thermal gradients in the thickness of the composite. Fig. 11a, b shows that the same temperature profiles are obtained on both sides demonstrating a good heating uniformity in the thickness of the flat and curved sample. By increasing the applied voltage, also in this case, the steady-state temperature tends to increase. To achieve the same heating performance (similar T_{ss}) as the G3 heater (see Fig. 10) higher voltage values were needed due to the thermal resistance of the fiberglass plies. Throughout the complete heating test for both fiberglass composites, the sample surface displays a uniform temperature distribution, as shown in the thermal maps at the higher applied voltage. Even in the case of the 3D-printed heater integrated into a fiberglass structure, the homogeneity of the thermal map means that no defects occurred in the heater during the integration procedure and the curing phase. The challenging aspect worth underlining is that even the prolonged printed contact underwent no modification. It follows that another advantage of using the FFF process is the possibility of printing the electrical contact directly together with the heater reducing the issues related to the scale-up at the industrial level of integrated electrothermal heaters. In view of real applications, further challenges remain to address, such as the use of high-performance polymers. It could be interesting to experiment with this approach with highly advanced engineering polymers, such as PEEK, PPS or PEI, which are widely investigated in the aerospace sector and for wind turbine blades [78]. In this way, high temperatures could be reached during the Joule heating, especially if this kind of versatile heater would be applied for the thermal curing of thermoset composites as out of autoclave process.

3.4. Joule heating modeling

To support experimental data, FEM analysis has been successfully carried out and presented hereafter.

The heat due to the Joule heating (JH) term can be expressed by Eq. (5):

$$Q_{JH} = J \cdot E = \frac{I}{CS} E = \frac{I^2}{CS} R = \frac{1}{\sigma} J^2 \tag{5}$$

Where J (A/m^2) is the current density expressed as the ratio between the current, I, flowing through the conductor and its cross-sectional area and σ(S/m) is the electrical conductivity. Therefore, the heat balance equation in the transient analysis could be written as Eq. (6):

$$\rho C_p \frac{\partial T}{\partial t} \nabla \cdot (k \nabla T) = Q_{JH} \tag{6}$$

The analysis is carried out by coupling the heat transfer physics and

Table 3
Materials' properties considered in the 3D model developed.

Parameters	Value	Unit	Description	Refs.
ρ_{ABS}	1090	kg/m^3	ABS/CNT Density	TDS$_{ABS}$ [79]
k_{ABS}	0.2	W/(m·K)	ABS/CNT Thermal conductivity	[51]
C_{pABS}	1400	J/(kg·K)	ABS/CNT Heat capacity	[80,81]
σ_{ABS}	1 ± 0.3	S/m	ABS/CNT Electrical conductivity	Present work
ρ_{Silver}	10,500	kg/m^3	Silver Density	[82]
k_{Silver}	9.1	W/(m·K)	Silver Thermal conductivity	[83]
$C_{pSilver}$	700	J/(kg·K)	Silver Heat capacity	[84]
σ_{Silver}	1e5	S/m	Silver electrical conductivity	TDS$_{Silver}$ [85]
h_∞	10	W/(m^2·K)	Convective heat flux coefficient	[28]

the electric current physics to account for the balance between the current flow inside the heater and its warming due to the rise of the Joule heating phenomenon.

The model reproduced the actual heater geometry, where the 3D printed system was decorated with conductive paint to create a current flow path. Therefore, the FEM model was defined by adding on the discretized geometry an additional layer (whose thickness was assumed to be 100 μm) according to the Fig. 1 configurations. The effectiveness of the analysis was verified by investigating the reliability of the analysis, analysing the effect of the conductive layer thickness and conductivity.

The analysis revealed that the Joule heating is properly triggered as long as the conductive layer has an electrical conductivity higher than ABS-CNT bulk materials. The layer thickness has a weak effect on the electrothermal behaviour.

The ABS-CNT was modeled as a homogeneous material; this assumption is compliant with its microstructure (Fig. 5) since the printing path was set to place side by side with each layer to promote the orientation of the filler, and it is homogeneously reproduced along the material section.

On the basis of these equations, FEM analysis was performed on the optimized G3 heater and GFRP/G3. For both samples, their variation of electrical resistance with temperature during the Joule heating test was considered negligible. According to the actual heater configuration (Fig. 12a, b), a layer of silver paste (thickness 0.1mm) was also considered. Fig. 12 depicts the CAD model of G3 used in COMSOL Multiphysics in its two domains: the ABS-CNT domain constituting the whole heater and the silver paste domain added on the equipotential surfaces to have the same potential difference at the extremes of each branch (Fig. 12b). Moreover, an electric potential of 18 V is applied to one electrodewhile a 0 V is considered (ground connection) on the other (Fig. 12a) according to the comb structure of the electrodes. As boundary conditions, the heater is assumed to be immersed in air, and the heat exchange conditions are based on natural convection.

The volume has been discretized as hexahedral elements whose material properties were obtained from the technical data sheet (TDS) and literature papers for ABS-CNT properties, while for silver paste, the information on the thermal properties was obtained by comparing different technical data sheets of commercial products. All the properties of the materials are reported in Table 3. The input voltage (18.2 V) and the properties of the materials were set in COMSOL Multiphysics as simulation parameters.

The problem was solved as a coupled electrical-thermal by finite elements as follows. A time-dependent study has been implemented from 0 to 1200 s. The electrical module was set up to evaluate the resistive heat generation rate, Q (W/m^3) as a function of the input voltage. Then the generation rate is provided to the thermal module. Two types of heat losses have been considered: (i) convective heat flux between the hot surface and surrounding air and (ii) conductive heat flux through adjacent materials. The simulated heat source consists of Joule heating generated by the electric current flowing through the 3D-printed model, between the electrodes path (Fig. 12a). The initial temperature of the system was set as the ambient temperature at 20 °C according to the experimental test. The thermal convection between the 3D-printed heater and the environment was defined with the convective heat flux (h) on the boundaries of the whole geometry.

The results of the simulation are shown in Fig. 13a, b. An electro-thermal coupling behavior of the 3D heater has been obtained due to the Joule heating: the temperature gradient corresponds to a difference in electrical potential inside the G3 heater.

Fig. 13a shows the numerical temperature profile of the point experimentally measured by a thermocouple. By the curve, it is possible to note a significant temperature rise (20–76 °C) in the heater. The temperature initially increases and then gets saturated, after about 130 s. Saturation of temperature indicates the establishment of thermal equilibrium, which depends on the balancing of heat generation through Joule heating and the dissipation of heat by convection and conduction.

Fig. 13a shows the heating history of the same point, comparing numerical and experimental results; the max temperature difference on the temperature between FEM predictions and experiment is about 1 ± 1 °C, then the model is quietly accurate for modeling the electro-thermal coupling behavior of the 3D printed heater. Thermal camera images capturing the surface temperature of the real sample were compared with the numerical model results at the same instant time (1200s), as shown in Fig. 13b.

In addition, a FEM analysis was performed on the G3 heater embedded in a fiberglass composite (GFRP) named GFRP/G3. The

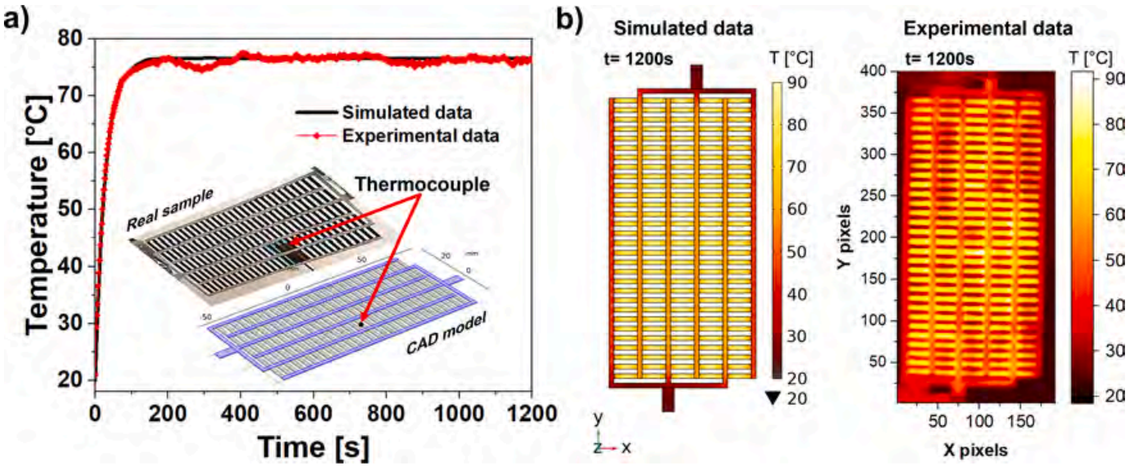

Fig. 13. Comparison between numerical and experimental results of Joule heating test of G3 heater: (a) temperature profiles; (b) Joule heating maps.

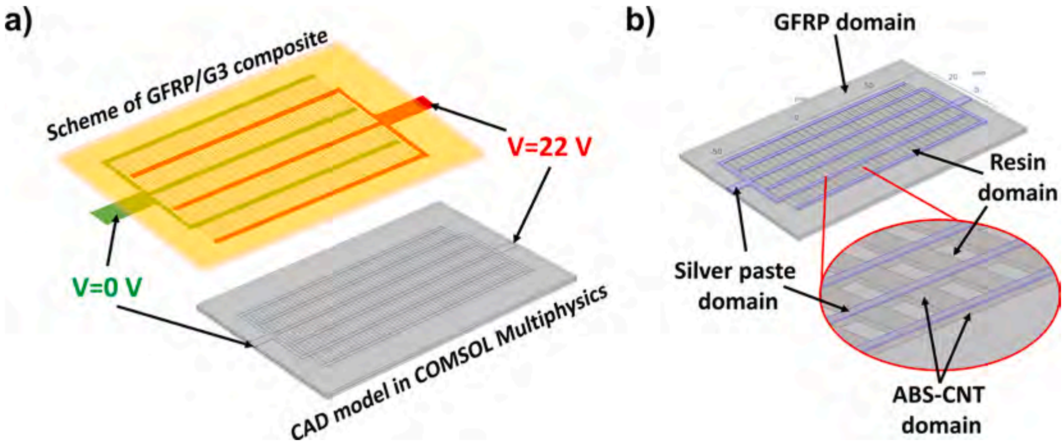

Fig. 14. (a) Scheme of electrical contacts on CAD model of GFRP/G3 in COMSOL Multiphysics, (b) ABS-CNT, silver paste, resin and GFRP domains.

Table 4
GFRP properties considered in the GFRP/G3.

Parameters	Value	Unit	Description	Refs.
ρ_{GFRP}	1900	kg/m^3	GFRP Density	[86]
k_{GFRP}	0.13	W/(m·K)	GFRP Thermal conductivity	[87]
C_{pGFRP}	1000	J/(kg·K)	GFRP Heat capacity	[87]
σ_{GFRP}	10e-9	S/m	GFRP Electrical conductivity	[86]

procedure set up previously has been implemented on the GFRP/G3 heater geometry. Fig. 14a shows the CAD model of the integrated system while Fig. 14b depicts the four domains constituting the GFRP/G3 model: ABS-CNT (the material of the G3 embedded heater), silver paste (for electrical contact on the surface of the G3 embedded heater), GFRP (external plies) and resin. About this latter domain, since the 3D-printed heater is placed in the middle section, the free volume between the branches heater has been considered filled by the resin of GFRP that penetrated into these cavities during the manufacturing process (see Fig. 3b) under the compaction effect of the vacuum bag. By a thermal point of view, GFRP and resin alone have similar parameters. An electric potential of 22V is applied to one electrode while a 0 V is considered (ground connection) on the other (Fig. 14). As boundary conditions, the fiberglass composite is considered immersed in air, and the heat exchange conditions are based on natural convection, as previously. The heat exchange between the heater and GFRP is by thermal conduction.

Material properties for the fiberglass material were obtained from the technical data sheet (TDS), and they are reported in Table 4, while the heater parameters were collected in Table 3.

The problem was solved as stated above. The initial temperature of the system was set as the ambient temperature at 28 °C according to the experiment. The results of the simulation are shown compared with the experimental ones in Fig. 15a, b.

The general behavior is similar to the bare G3 heater immersed in air with an equilibrium temperature of 77 °C. In order to achieve an equilibrium temperature similar to the bare heater system a higher power supply was required to account for the high energy requested to warm also the surrounding GFRP. Fig. 15a shows the heating history of the same point measured experimentally with a thermocouple, comparing numerical and experimental results. Also the model of the embedded system shows a good agreement with the experimental test, in fact, the max temperature difference measured and the temperature FEM predicted is about 1 ± 1 °C.

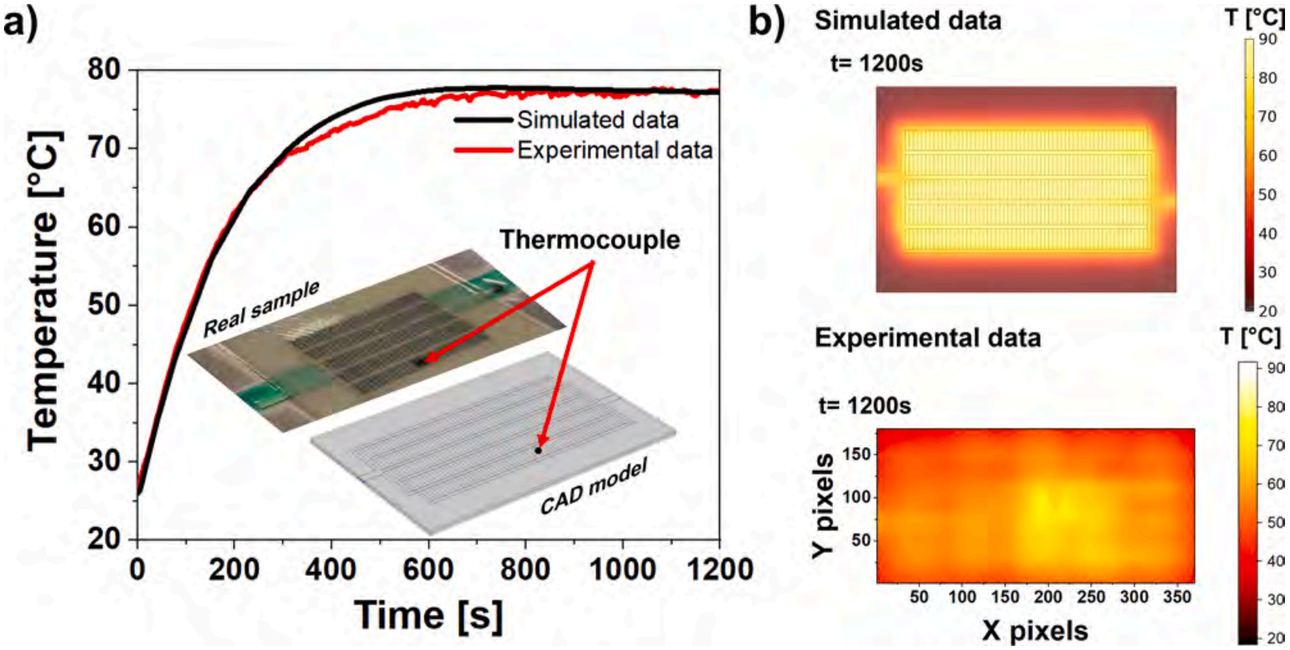

Fig. 15. Comparison between numerical and experimental results of Joule heating test of GFRP/G3 sample: (a) temperature profiles; (b) Joule heating maps.

4. Conclusions

In this work, ABS modified by CNT has been printed via the FFF process to obtain a heating resistor tunable according to required specifics, such as steady state temperature, power source available in the application field, and, eventually, flexibility and scalability.

A design strategy for optimizing the electrical performance of the element has been discussed and experimentally validated. The electrical resistance has been reduced from about 30 kΩ to 30 Ω by properly setting FFF process parameters (such as the infill pattern) and the geometric parameters of the heater (length, width, thickness, and number of resistive branches in parallel). The used approach allowed for the successful integration of the optimized heater into the curved fiberglass composite whose Joule heating performance was experimentally carried out and simulated by multi-physics FEM analysis obtaining a good accordance of the data. This work enables the design of functional patches that could be employed in several fields for inducing active thermal management (i.e., de-icing, smart tools, etc.…), adaptable to part curvature and prone to integration within structural elements.

CRediT authorship contribution statement

Francesca Aliberti: Writing – review & editing, Writing – original draft, Methodology, Investigation, Formal analysis, Data curation, Conceptualization. **Andrea Sorrentino:** Resources, Methodology, Data curation. **Barbara Palmieri:** Software, Formal analysis, Data curation. **Luigi Vertuccio:** Writing – review & editing, Validation, Methodology, Investigation. **Giuseppe De Tommaso:** Resources. **Roberto Pantani:** Visualization, Data curation. **Liberata Guadagno:** Writing – review & editing, Supervision, Funding acquisition, Conceptualization. **Alfonso Martone:** Writing – review & editing, Supervision, Formal analysis, Data curation.

Declaration of competing interest

The authors declare that they have no known competing financial interests or personal relationships that could have appeared to influence the work reported in this paper.

Acknowledgments

The research leading to these results is funded by the CENTRO NAZIONALE DI RICERCA PER LA MOBILITA' SOSTENIBILE - CNMS - CN00000023 - AFFILIATO SPOKE 2 - Sustainable road vehicle (POLITO) and by the Italian Ministry of University and Research - PRIN 2022 project “Integration of Continuous Fibers and Self-Healing Agents in 3D Printed Thermoplastic Composites (INFINITE)” (Prot. 2022AKTCPH).

Supplementary materials

Supplementary material associated with this article can be found, in the online version, at doi:10.1016/j.jcomc.2024.100527.

Data availability

Data will be made available on request.

References

[1] A. Tinti, G.A. Carallo, A. Greco, M.D. Romero-Sánchez, L. Vertuccio, L. Guadagno, Effective practical solutions for de-icing of automotive component, Nanomaterials 12 (2022) 2979, https://doi.org/10.3390/nano12172979.

[2] X. Guo, Q. Yang, H. Zheng, W. Dong, Integrated composite electrothermal de-icing system based on ultra-thin flexible heating film, Appl. Therm. Eng. 236 (2024) 121723, https://doi.org/10.1016/J.APPLTHERMALENG.2023.121723.

[3] K. Wei, Y. Yang, H. Zuo, D. Zhong, A review on ice detection technology and ice elimination technology for wind turbine, Wind Energy 23 (2020) 433–457, https://doi.org/10.1002/WE.2427.

[4] P.O.A. Borrebæk, B.P. Jelle, Z. Zhang, Avoiding snow and ice accretion on building integrated photovoltaics – challenges, strategies, and opportunities, Sol. Energy Mater. Sol. Cells 206 (2020) 110306, https://doi.org/10.1016/J.SOLMAT.2019.110306.

[5] L. Gao, T. Tao, Y. Liu, H. Hu, A field study of ice accretion and its effects on the power production of utility-scale wind turbines, Renew. Energy 167 (2021) 917–928, https://doi.org/10.1016/J.RENENE.2020.12.014.

[6] G. Prasad, J. Bruce Ralphin Rose, Experimental and computational study of ice accretion effects on aerodynamic performance, Aircr. Eng. Aerosp. Technol. 92 (2020) 827–836, https://doi.org/10.1108/AEAT-03-2019-0039.

[7] Z. Wu, Q. Wang, Effect of and protection from ice accretion on aircraft. Ice AdhesionMechanism, Measurement and Mitigation, 2020, pp. 577–606. https://doi.org/10.1002/9781119640523.ch19.

[8] C. Yue, Y. Zhang, W. Lu, Y. Zhang, P. Wang, Y. Li, H. Zhou, Realizing the curing of polymer composite materials by using electrical resistance heating: a review, Compos. Part A Appl. Sci. Manuf. 163 (2022) 107181, https://doi.org/10.1016/J.COMPOSITESA.2022.107181.

[9] B. Zhang, Y. Li, S. Liu, Y. Shen, X. Hao, Layered self-resistance electric heating to cure thick carbon fiber reinforced epoxy laminates, Polym. Compos. 42 (2021) 2469–2483, https://doi.org/10.1002/PC.25992.

[10] M. Anas, M.M. Mustafa, D.G. Carey, A. Sarmah, J.J. LeMonte, M.J. Green, Joule heating of carbon pixels for on-demand thermal patterning, Carbon 174 (2021) 518–523, https://doi.org/10.1016/J.CARBON.2020.12.054. N. Y.

[11] B.M. Gackowski, M. Sharma, S. Idapalapati, Multi-material additive manufacturing of self-heating structures for out-of-autoclave post-processing and de-icing, Addit. Manuf 68 (2023) 103519, https://doi.org/10.1016/j.addma.2023.103519.

[12] D. Brassard, M. Dubé, J.R. Tavares, Modelling resistance welding of thermoplastic composites with a nanocomposite heating element, J. Compos. Mater. 55 (2021) 625–639, https://doi.org/10.1177/0021998320957055.

[13] D. Brassard, M. Dubé, J.R. Tavares, Resistance welding of thermoplastic composites with a nanocomposite heating element, Compos. B Eng. 165 (2019) 779–784, https://doi.org/10.1016/J.COMPOSITESB.2019.02.038.

[14] H. Frederick, W. Li, G. Palardy, Disassembly study of ultrasonically welded thermoplastic composite joints via resistance heating, Materials 14 (2021) 2521, https://doi.org/10.3390/MA14102521.

[15] X. Xiong, D. Wang, J. Wei, P. Zhao, R. Ren, J. Dong, X. Cui, Resistance welding technology of fiber reinforced polymer composites: a review, J. Adhes. Sci. Technol. 35 (2021) 1593–1619, https://doi.org/10.1080/01694243.2020.1856514.

[16] B.H.A.H. Tijs, M.H.J. Doldersum, A. Turon, J.E.A. Waleson, C. Bisagni, Experimental and numerical evaluation of conduction welded thermoplastic composite joints, Compos. Struct. 281 (2022) 114964, https://doi.org/10.1016/J.COMPSTRUCT.2021.114964.

[17] T. Xia, D. Zeng, Z. Li, R.J. Young, C. Vallés, I.A. Kinloch, Electrically conductive GNP/epoxy composites for out-of-autoclave thermoset curing through Joule heating, Compos. Sci. Technol. 164 (2018) 304–312, https://doi.org/10.1016/J.COMPSCITECH.2018.05.053.

[18] L. Guadagno, A. Sorrentino, P. Delprat, L. Vertuccio, Design of multifunctional composites: new strategy to save energy and improve mechanical performance, Nanomaterials 10 (2020) 2285, https://doi.org/10.3390/NANO10112285.

[19] B. Palmieri, A. Petriccione, G. De Tommaso, M. Giordano, A. Martone, An efficient thermal cure profile for thick parts made by reactive processing of acrylic thermoplastic composites, J. Compos. Sci. 5 (2021) 229, https://doi.org/10.3390/JCS5090229.

[20] T.J. Ahmed, D. Stavrov, H.E.N. Bersee, A. Beukers, Induction welding of thermoplastic composites—An overview, Compos. Part A Appl. Sci. Manuf. 37 (2006) 1638–1651, https://doi.org/10.1016/J.COMPOSITESA.2005.10.009.

[21] T. Segreto, A. Bottillo, B. Palmieri, L. Nele, R. Teti, Ultrasonic evaluation of induction heat treatment applied to thermoplastic matrix CFRP, Procedia CIRP 88 (2020) 467–472, https://doi.org/10.1016/J.PROCIR.2020.05.081.

[22] Y. Xia, P. Cai, Y. Liu, J. Zhu, R. Guo, W. Zhang, Y. Gan, H. Huang, J. Zhang, C. Liang, X. He, Z. Xiao, A low-cost and high-efficiency electrothermal composite film composed of hybrid conductivity fillers and polymer blends matrix for high-performance plate heater, J. Electron. Mater. 50 (2021) 3084–3094, https://doi.org/10.1007/s11664-021-08873-0.

[23] D. Janas, K.K. Koziol, A review of production methods of carbon nanotube and graphene thin films for electrothermal applications, Nanoscale 6 (2014) 3037–3045, https://doi.org/10.1039/C3NR05636H.

[24] C. Yue, Y. Zhang, W. Lu, Y. Zhang, P. Wang, Y. Li, H. Zhou, Realizing the curing of polymer composite materials by using electrical resistance heating: a review, Compos. Part A Appl. Sci. Manuf. 163 (2022) 107181, https://doi.org/10.1016/J.COMPOSITESA.2022.107181.

[25] A. Cortés, X.F. Sánchez Romate, A. Jiménez-Suárez, M. Campo, M.G. Prolongo, A. Ureña, S.G. Prolongo, 3D printed anti-icing and de-icing system based on CNT/GNP doped epoxy composites with self-curing and structural health monitoring capabilities, Smart Mater. Struct. 30 (2020) 025016, https://doi.org/10.1088/1361-665X/ABD343.

[26] T. Rashid, H.L. Liang, M. Taimur, N. Chiodarelli, H.A. Khawaja, K. Edvardsen, M. de Volder, Roll to roll coating of carbon nanotube films for electro thermal heating, Cold Reg. Sci. Technol. 182 (2021) 103210, https://doi.org/10.1016/J.COLDREGIONS.2020.103210.

[27] Z. Zhao, H. Chen, X. Liu, Z. Wang, Y. Zhu, Y. Zhou, Novel sandwich structural electric heating coating for anti-icing/de-icing on complex surfaces, Surf. Coat. Technol. 404 (2020) 126489, https://doi.org/10.1016/J.SURFCOAT.2020.126489.

[28] L. Guadagno, L. Vertuccio, F. Foglia, M. Raimondo, G. Barra, A. Sorrentino, R. Pantani, E. Calabrese, Flexible eco-friendly multilayer film heaters, Compos. B Eng. 224 (2021) 109208, https://doi.org/10.1016/J.COMPOSITESB.2021.109208.

[29] J. Chen, Y. Wang, F. Liu, S. Luo, Laser-induced graphene paper heaters with multimodally patternable electrothermal performance for low-energy manufacturing of composites, ACS Appl. Mater. Interfaces 12 (2020) 23284–23297, https://doi.org/10.1021/ACSAMI.0C02188.

[30] F. Cilento, A. Martone, M.G. Pastore Carbone, C. Galiotis, M. Giordano, Nacre-like GNP/Epoxy composites: reinforcement efficiency vis-à-vis graphene content, Compos. Sci. Technol. 211 (2021) 108873, https://doi.org/10.1016/J.COMPSCITECH.2021.108873.

[31] C. Leone, M. Di Siena, S. Genna, A. Martone, Effect of graphite nanoplatelets percentage on the in plane thermal diffusivity of ultra-thin graphene based (nanostructured) composite, Opt. Laser Technol. 146 (2022) 107552, https://doi.org/10.1016/J.OPTLASTEC.2021.107552.

[32] H. Wu, F. Shi, Z. Zhang, Z. Zhong, X. Wei, Effect of carbon fiber bundles spacing on composites and their electrothermal and anti/deicing properties, Mater. Sci. Eng. B 299 (2024) 117021, https://doi.org/10.1016/J.MSEB.2023.117021.

[33] L.C. Kontaxis, I.E. Chontzoglou, G.C. Papanicolaou, L. Valentini, T. Sadowski, L. Marsavina, Efficient use of carbon fibers as heating elements for curing of epoxy matrix composites, Molecules 26 (2021) 5095, https://doi.org/10.3390/MOLECULES26165095.

[34] P. Blyweert, V. Nicolas, V. Fierro, A. Celzard, 3D printing of carbon-based materials: a review, Carbon 183 (2021) 449–485, https://doi.org/10.1016/J.CARBON.2021.07.036. N. Y.

[35] A. Cortés, X.F. Sánchez Romate, A. Jiménez-Suárez, M. Campo, M.G. Prolongo, A. Ureña, S.G. Prolongo, 3D printed anti-icing and de-icing system based on CNT/GNP doped epoxy composites with self-curing and structural health monitoring capabilities, Smart Mater. Struct. 30 (2020) 025016, https://doi.org/10.1088/1361-665X/ABD343.

[36] A.M. Rezaei, R. Izadi, N. Fantuzzi, A hierarchical nano to micro scale modelling of 3D printed nano-reinforced polylactic acid: micropolar modelling and molecular dynamics simulation, Nanomaterials 14 (2024) 1113, https://doi.org/10.3390/NANO14131113.

[37] N. Vidakis, M. Petousis, E. Velidakis, N. Mountakis, S. Grammatikos, L. Tzounis, Multi-functional medical grade Polyamide12/Carbon black nanocomposites in material extrusion 3D printing, Compos. Struct. 311 (2023) 116788, https://doi.org/10.1016/J.COMPSTRUCT.2023.116788.

[38] M. Lalegani Dezaki, M.K.A. Mohd Ariffin, S. Hatami, An overview of fused deposition modelling (FDM): research, development and process optimisation, Rapid Prototyp. J. 27 (2021) 562–582, https://doi.org/10.1108/RPJ-08-2019-0230.

[39] N. Vidakis, M. Petousis, E. Velidakis, N. Mountakis, P.E. Fischer-Griffiths, S. Grammatikos, L. Tzounis, Fused filament fabrication three-dimensional printing multi-functional of polylactic acid/carbon black nanocomposites, J. Carbon Res. 7 (2021) 52, https://doi.org/10.3390/C7030052.

[40] I. Tirado-Garcia, D. Garcia-Gonzalez, S. Garzon-Hernandez, A. Rusinek, G. Robles, J.M. Martinez-Tarifa, A. Arias, Conductive 3D printed PLA composites: on the interplay of mechanical, electrical and thermal behaviours, Compos. Struct. 265 (2021) 113744, https://doi.org/10.1016/J.COMPSTRUCT.2021.113744.

[41] L. Yang, X. Liu, Y. Xiao, B. Liu, Z. Xue, Y. Wang, Additive manufacturing of carbon nanotube/polylactic acid films with efficient electromagnetic interference shielding and electrical heating performance via fused deposition modeling, Synth. Met. 293 (2023) 117258, https://doi.org/10.1016/J.SYNTHMET.2022.117258.

[42] K.B. Mustapha, K.M. Metwalli, A review of fused deposition modelling for 3D printing of smart polymeric materials and composites, Eur. Polym. J. 156 (2021) 110591, https://doi.org/10.1016/J.EURPOLYMJ.2021.110591.

[43] J. Jyoti, S. Basu, B.P. Singh, S.R. Dhakate, Superior mechanical and electrical properties of multiwall carbon nanotube reinforced acrylonitrile butadiene styrene high performance composites, Compos. B Eng. 83 (2015) 58–65, https://doi.org/10.1016/J.COMPOSITESB.2015.08.055.

[44] N. Vidakis, A. Maniadi, M. Petousis, M. Vamvakaki, G. Kenanakis, E. Koudoumas, Mechanical and electrical properties investigation of 3D-printed acrylonitrile–butadiene–styrene graphene and carbon nanocomposites, J. Mater. Eng. Perform. 29 (2020) 1909–1918, https://doi.org/10.1007/s11665-020-04689-x.

[45] N. Vidakis, M. Petousis, L. Tzounis, E. Velidakis, N. Mountakis, S.A. Grammatikos, Polyamide 12/multiwalled carbon nanotube and carbon black nanocomposites manufactured by 3D printing fused filament fabrication: a comparison of the electrical, thermoelectric, and mechanical properties, J. Carbon Res. 7 (2021) 38, https://doi.org/10.3390/C7020038.

[46] N. Vidakis, M. Petousis, E. Velidakis, L. Tzounis, N. Mountakis, O. Boura, S. A. Grammatikos, Multi-functional polyamide 12 (PA12)/multiwall carbon nanotube 3D printed nanocomposites with enhanced mechanical and electrical properties, Adv. Compos. Mater. 31 (2022) 630–654, https://doi.org/10.1080/09243046.2022.2076019.

[47] N. Vidakis, M. Petousis, M. Kourinou, E. Velidakis, N. Mountakis, P.E. Fischer-Griffiths, S. Grammatikos, L. Tzounis, Additive manufacturing of multifunctional polylactic acid (PLA)—Multiwalled carbon nanotubes (MWCNTs) nanocomposites, Nanocomposites 7 (2021) 184–199, https://doi.org/10.1080/20550324.2021.2000231.

[48] L. Tzounis, M. Petousis, S. Grammatikos, N. Vidakis, 3D printed thermoelectric polyurethane/multiwalled carbon nanotube nanocomposites: a novel approach towards the fabrication of flexible and stretchable organic thermoelectrics, Materials 13 (2020) 2879, https://doi.org/10.3390/MA13122879.

[49] N.A. Fountas, I. Papantoniou, J.D. Kechagias, D.E. Manolakos, N.M. Vaxevanidis, Modeling and optimization of flexural properties of FDM-processed PET-G specimens using RSM and GWO algorithm, Eng. Fail. Anal. 138 (2022) 106340, https://doi.org/10.1016/J.ENGFAILANAL.2022.106340.

[50] S.G. Prolongo, R. Moriche, G. Del Rosario, A. Jiménez-Suárez, M.G. Prolongo, A. Ureña, Joule effect self-heating of epoxy composites reinforced with graphitic nanofillers, J. Polym. Res. 23 (2016) 1–7, https://doi.org/10.1007/s10965-016-1092-4.

[51] L. Guadagno, F. Aliberti, R. Longo, M. Raimondo, R. Pantani, A. Sorrentino, M. Catauro, L. Vertuccio, Electrical anisotropy controlled heating of acrylonitrile butadiene styrene 3D printed parts, Mater. Des. 225 (2023) 111507, https://doi.org/10.1016/J.MATDES.2022.111507.

[52] S. Dul, B.J.A. Gutierrez, A. Pegoretti, J. Alvarez-Quintana, L. Fambri, 3D printing of ABS nanocomposites. Comparison of processing and effects of multi-wall and single-wall carbon nanotubes on thermal, mechanical and electrical properties, J. Mater. Sci. Technol. 121 (2022) 52–66, https://doi.org/10.1016/J.JMST.2021.11.064.

[53] W.Y. Wang, G.H. Luo, F. Wei, J. Luo, Electrical conductivity and thermal properties of acrylonitrile-butadiene-styrene filled with multiwall carbon nanotubes, Polym. Eng. Sci. 49 (2009) 2144–2149, https://doi.org/10.1002/PEN.21454.

[54] Y. Ming, Y. Duan, S. Zhang, Y. Zhu, B. Wang, Self-heating 3D printed continuous carbon fiber/epoxy mesh and its application in wind turbine deicing, Polym. Test. 82 (2020) 106309, https://doi.org/10.1016/J.POLYMERTESTING.2019.106309.

[55] L. Diatezo, M.Q. Le, C. Tonellato, L. Puig, J.F. Capsal, P.J. Cottinet, Development and optimization of 3D-printed flexible electronic coatings: a new generation of smart heating fabrics for automobile applications, Micromachines 14 (2023) 762, https://doi.org/10.3390/MI14040762 (Basel).

[56] N. Fountas, J. Kechagias, N. Vaxevanidis, Statistical modeling and optimization of surface roughness for PLA and PLA/Wood FDM fabricated items, J. Mater. Eng. 1 (2023) 38–44, https://doi.org/10.61552/JME.2023.01.005.

[57] N.A. Fountas, K. Kitsakis, K.E. Aslani, J.D. Kechagias, N.M. Vaxevanidis, An experimental investigation of surface roughness in 3D-printed PLA items using design of experiments, Proc. Inst. Mech. Eng. Part J J. Eng. Tribol. 236 (2021) 1979–1984, https://doi.org/10.1177/13506501211059306.

[58] J.D. Kechagias, Surface roughness assessment of ABS and PLA filament 3D printing parts: structural parameters experimentation and semi-empirical modelling, Int. J. Adv. Manuf. Technol. 134 (2024) 1935–1946, https://doi.org/10.1007/s00170-024-14232-0.

[59] J.D. Kechagias, N. Vidakis, K. Ninikas, M. Petousis, N.M. Vaxevanidis, Hybrid 3D printing of multifunctional polylactic acid/carbon black nanocomposites made with material extrusion and post-processed with CO$_2$ laser cutting, Int. J. Adv. Manuf. Technol. 124 (2023) 1843–1861, https://doi.org/10.1007/S00170-022-10604-6.

[60] J. Kechagias, S. Zaoutsos, Effects of 3D-printing processing parameters on FFF parts' porosity: outlook and trends, Mater. Manuf. Process. 39 (2024) 804–814, https://doi.org/10.1080/10426914.2024.2304843.

[61] L. Paleari, M. Bragaglia, M. Mariani, F. Nanni, Acrylonitrile butadiene styrene – carbon nanotubes nanocomposites for 3D printing of health monitoring components, J. Reinf. Plast. Compos. 42 (2023) 857–870, https://doi.org/10.1177/07316844221141364.

[62] K.L. Snapp, A.E. Gongora, K.A. Brown, Increasing throughput in fused deposition modeling by modulating bed temperature, J. Manuf. Sci. Eng. Trans. ASME 143 (2021), https://doi.org/10.1115/1.4050177/1098804.

[63] Prepregs & UD-Prepregs | KREMPEL. https://krempel.com/en/products/composites/prepregs-ud-prepregs (accessed July 13, 2024).

[64] L. Guadagno, R. Longo, F. Aliberti, P. Lamberti, V. Tucci, R. Pantani, G. Spinelli, M. Catauro, L. Vertuccio, Role of MWCNTs loading in designing self-sensing and self-heating structural elements, Nanomaterials 13 (2023) 495, https://doi.org/10.3390/NANO13030495.

[65] S. Dul, B.J.A. Gutierrez, A. Pegoretti, J. Alvarez-Quintana, L. Fambri, 3D printing of ABS nanocomposites. Comparison of processing and effects of multi-wall and single-wall carbon nanotubes on thermal, mechanical and electrical properties, J. Mater. Sci. Technol. 121 (2022) 52–66, https://doi.org/10.1016/J.JMST.2021.11.064.

[66] T. Sonsalla, A.L. Moore, A.D. Radadia, L. Weiss, Printer orientation effects and performance of novel 3-D printable acrylonitrile butadiene styrene (ABS) composite filaments for thermal enhancement, Polym. Test. 80 (2019) 106125, https://doi.org/10.1016/J.POLYMERTESTING.2019.106125.

[67] H.S. Patanwala, D. Hong, S.R. Vora, B. Bognet, A.W.K. Ma, The microstructure and mechanical properties of 3D printed carbon nanotube-polylactic acid composites, Polym. Compos. 39 (2018) E1060–E1071, https://doi.org/10.1002/PC.24494.

[68] Y. Jia, H. He, Y. Geng, B. Huang, X. Peng, High through-plane thermal conductivity of polymer based product with vertical alignment of graphite flakes achieved via 3D printing, Compos. Sci. Technol. 145 (2017) 55–61, https://doi.org/10.1016/J.COMPSCITECH.2017.03.035.

[69] Y. Qian, C. Li, Y. Qi, J. Zhong, 3D printing of graphene oxide composites with well controlled alignment, Carbon 171 (2021) 777–784, https://doi.org/10.1016/J.CARBON.2020.08.077. N. Y.

[70] H. Schefer, L. Fauth, T.H. Kopp, R. Mallwitz, J. Friebe, M. Kurrat, Discussion on electric power supply systems for all electric aircraft, IEEE Access 8 (2020) 84188–84216, https://doi.org/10.1109/ACCESS.2020.2991804.

[71] A.G. Mohammed, G. Ozgur, E. Sevkat, Electrical resistance heating for deicing and snow melting applications: experimental study, Cold Reg. Sci. Technol. 160 (2019) 128–138, https://doi.org/10.1016/J.COLDREGIONS.2019.02.004.

[72] D.R. Biba, S. Musuroi, M. Svoboda, Powertrain 48V power supply proposal and safety validation voltage levels for BLDC Motor Driver ASIC, in: Proceedings of the

2018 International Conference on Applied and Theoretical Electricity, ICATE, 2018, https://doi.org/10.1109/ICATE.2018.8551470.

[73] M. Al-Bahrani, J. Graham-Jones, Z. Gombos, A. Al-Ani, A. Cree, High-efficient multifunctional self-heating nanocomposite-based MWCNTs for energy applications, Int. J. Energy Res. 44 (2020) 1113–1124, https://doi.org/10.1002/ER.4999.

[74] S.H. Jang, Y.L. Park, Carbon nanotube-reinforced smart composites for sensing freezing temperature and deicing by self-heating, Nanomater. Nanotechnol. 8 (2018), https://doi.org/10.1177/1847980418776473.

[75] L. Yang, X. Liu, Y. Xiao, B. Liu, Z. Xue, Y. Wang, Additive manufacturing of carbon nanotube/polylactic acid films with efficient electromagnetic interference shielding and electrical heating performance via fused deposition modeling, Synth. Met. 293 (2023) 117258, https://doi.org/10.1016/J.SYNTHMET.2022.117258.

[76] H. Kim, S. Lee, Characterization of electrical heating performance of CFDM 3D-printed graphene/polylactic acid (PLA) horseshoe pattern with different 3D printing directions, Polymers 12 (2020) 2955, https://doi.org/10.3390/POLYM12122955 (Basel).

[77] H. Kim, S. Lee, Characterization of electrical heating of graphene/PLA honeycomb structure composite manufactured by CFDM 3D printer, Fash. Text. 7 (2020) 1–18, https://doi.org/10.1186/S40691-020-0204-2.

[78] A. El Magri, S. Vanaei, S. Vaudreuil, An overview on the influence of process parameters through the characteristic of 3D-printed PEEK and PEI parts, High Perform. Polym. 33 (2021) 862–880, https://doi.org/10.1177/09540083211009961.

[79] ESD ABS 3D Printing Filament, Made in the USA! | Static Discharge Printing, (accessed June 13, 2024). https://www.3dxtech.com/product/3dxstat-esd-abs/(accessed June 12, 2024).

[80] L. Bogaerts, M. Faes, J. Bergen, J. Cloots, E. Vasiliauskaite, F. Vogeler, D. Moens, Influence of thermo-mechanical loads on the lifetime of plastic inserts for injection moulds produced via additive manufacturing, Procedia CIRP 96 (2021) 109–114, https://doi.org/10.1016/J.PROCIR.2021.01.061.

[81] S. Clark, T. Yap, M. Tehrani, Validation of a Finite element model for fused filament fabrication additive manufacturing, in: Proceedings of the ASME International Mechanical Engineering Congress and Exposition (IMECE), 2022, https://doi.org/10.1115/IMECE2021-73803, 2A–2021.

[82] Silver Paste, AMERICAN ELEMENTS ®, https://www.americanelements.com/silver-paste-7440-22-4 (accessed June 13, 2024).

[83] PELCO ® High Performance Silver Paste, 50g, https://www.tedpella.com/technote_html/16047-TN-V1-06232009.pdf (accessed June 13, 2024).

[84] Anon, https://www.amecthermasol.co.uk/datasheets/Paste_Comparison.pdf, (accessed June 13, 2024).

[85] Anon, RS PRO silver conductive lacquer for PCB solder masking, high temperature applications, RS. https://nl.rs-online.com/web/p/electronics-varnishes/1863600 (accessed June 13, 2024).

[86] Materials data book, http://www-mdp.eng.cam.ac.uk/web/library/enginfo/cueddatabooks/materials.pdf (accessed July 13, 2024).

[87] Y. Bai, N.L. Post, J.J. Lesko, T. Keller, Experimental investigations on temperature-dependent thermo-physical and mechanical properties of pultruded GFRP composites, Thermochim. Acta 469 (2008) 28–35, https://doi.org/10.1016/J.TCA.2008.01.002.